UC Irvine
UC Irvine Previously Published Works

Title

Quantitative, depth-resolved determination of particle motion using multi-exposure, spatial frequency domain laser speckle imaging

Permalink

https://escholarship.org/uc/item/7xr4v331

Journal

Biomedical Optics Express, 4(12)

ISSN

2156-7085 2156-7085

Authors

Rice, Tyler B
Kwan, Elliott
Hayakawa, Carole K
et al.

Publication Date

2013-11-19

DOI

10.1364/BOE.4.002880

Copyright Information

Peer reviewed

Quantitative, depth-resolved determination of particle motion using multi-exposure, spatial frequency domain laser speckle imaging

Tyler B. Rice,[1,2] Elliott Kwan,[2] Carole K. Hayakawa[2], Anthony J. Durkin,[2] Bernard Choi,[2] and Bruce J. Tromberg[2,*]

[1] *Department of Physics, 4129 Frederick Reines Hall, University of California Irvine, Irvine, CA 92697 USA*
[2] *Laser Microbeam and Medical Program (LAMMP), Beckman Laser Institute, 1002 Health Sciences Road, Irvine, CA 92612, USA*
*bjtrombe@uci.edu

Abstract: Laser Speckle Imaging (LSI) is a simple, noninvasive technique for rapid imaging of particle motion in scattering media such as biological tissue. LSI is generally used to derive a qualitative index of relative blood flow due to unknown impact from several variables that affect speckle contrast. These variables may include optical absorption and scattering coefficients, multi-layer dynamics including static, non-ergodic regions, and systematic effects such as laser coherence length. In order to account for these effects and move toward quantitative, depth-resolved LSI, we have developed a method that combines Monte Carlo modeling, multi-exposure speckle imaging (MESI), spatial frequency domain imaging (SFDI), and careful instrument calibration. Monte Carlo models were used to generate total and *layer-specific fractional* momentum transfer distributions. This information was used to predict speckle contrast as a function of exposure time, spatial frequency, layer thickness, and layer dynamics. To verify with experimental data, controlled phantom experiments with characteristic tissue optical properties were performed using a structured light speckle imaging system. Three main geometries were explored: 1) diffusive dynamic layer beneath a static layer, 2) static layer beneath a diffuse dynamic layer, and 3) directed flow (tube) submerged in a dynamic scattering layer. Data fits were performed using the Monte Carlo model, which accurately reconstructed the type of particle flow (diffusive or directed) in each layer, the layer thickness, and absolute flow speeds to within 15% or better.

© 2013 Optical Society of America

OCIS codes: (110.6150) Speckle imaging; (170.3660) Light propagation in tissues.

References and links

1. B. J. Berne and R. Pecora, *Dynamic light scattering: with applications to chemistry, biology, and physics,* Dover ed. (Dover Publications, Mineola, N.Y., 2000), pp. vii, 376 p.
2. R. Pecora, *Dynamic light scattering: applications of photon correlation spectroscopy* (Plenum Press, New York, 1985), pp. xiv, 420 p.
3. A. Wax and V. Backman, *Biomedical applications of light scattering*, Biophotonics series (McGraw-Hill, New York, 2010), pp. xv, 368 p., 316 p. of plates.
4. G. E. Nilsson, T. Tenland, and P. A. Oberg, "Evaluation of a laser Doppler flowmeter for measurement of tissue blood flow," IEEE Trans. Biomed. Eng. **27**(10), 597–604 (1980).
5. M. H. Koelink, F. F. M. de Mul, J. Greve, R. Graaff, A. C. M. Dassel, and J. G. Aarnoudse, "Laser Doppler blood flowmetry using two wavelengths: Monte Carlo simulations and measurements," Appl. Opt. **33**(16), 3549–3558 (1994).
6. P. A. Oberg, "Laser-Doppler flowmetry," Crit. Rev. Biomed. Eng. **18**(2), 125–163 (1990).
7. D. J. Pine, D. A. Weitz, P. M. Chaikin, and E. Herbolzheimer, "Diffusing wave spectroscopy," Phys. Rev. Lett. **60**(12), 1134–1137 (1988).

8. D. J. Pine, D. A. Weitz, J. X. Zhu, and E. Herbolzheimer, "Diffusing-wave spectroscopy: dynamic light scattering in the multiple scattering limit," J. Phys. (Paris) **51**(18), 2101–2127 (1990).
9. D. J. Durian, "Accuracy of diffusing-wave spectroscopy theories," Phys. Rev. E Stat. Phys. Plasmas Fluids Relat. Interdiscip. Topics **51**(4), 3350–3358 (1995).
10. D. A. Boas and A. G. Yodh, "Spatially varying dynamical properties of turbid media probed with diffusing temporal light correlation," J. Opt. Soc. Am. A **14**(1), 192–215 (1997).
11. B. Choi, N. M. Kang, and J. S. Nelson, "Laser speckle imaging for monitoring blood flow dynamics in the in vivo rodent dorsal skin fold model," Microvasc. Res. **68**(2), 143–146 (2004).
12. A. F. Fercher and J. D. Briers, "Flow visualization by means of single-exposure speckle photography," Opt. Commun. **37**(5), 326–330 (1981).
13. J. D. Briers, G. Richards, and X. W. He, "Capillary Blood Flow Monitoring Using Laser Speckle Contrast Analysis (LASCA)," J. Biomed. Opt. **4**(1), 164–175 (1999).
14. R. Bandyopadhyay, A. S. Gittings, S. S. Suh, P. K. Dixon, and D. J. Durian, "Speckle-visibility spectroscopy: A tool to study time-varying dynamics," Rev. Sci. Instrum. **76**(9), 093110–093111 (2005).
15. D. A. Boas and A. K. Dunn, "Laser speckle contrast imaging in biomedical optics," J. Biomed. Opt. **15**(1), 011109–011112 (2010).
16. M. S. Singh, K. Rajan, and R. M. Vasu, "Estimation of elasticity map of soft biological tissue mimicking phantom using laser speckle contrast analysis," J. Appl. Phys. **109**, 104704 (2011).
17. R. L. Dougherty, B. J. Ackerson, N. M. Reguigui, F. Dorri-Nowkoorani, and U. Nobbmann, "Correlation transfer: Development and application," J. Quantum Spectrosc. Radiative Transf. **52**(6), 713–727 (1994).
18. N. Dögnitz and G. Wagnières, "Determination of tissue optical properties by steady-state spatial frequency-domain reflectometry," Lasers Med. Sci. **13**, 55–65 (1998).
19. D. Cuccia, B. Tromberg, R. Frostig, and D. Abookasis, "Quantitative In Vivo Imaging of Tissue Absorption, Scattering, and Hemoglobin Concentration in Rat Cortex Using Spatially Modulated Structured Light," in *In Vivo Optical Imaging of Brain Function, Second Edition* (CRC Press, 2009), pp. 339–361.
20. D. J. Cuccia, F. Bevilacqua, A. J. Durkin, F. R. Ayers, and B. J. Tromberg, "Quantitation and mapping of tissue optical properties using modulated imaging," J. Biomed. Opt. **14**(2), 024012 (2009).
21. D. J. Cuccia, F. Bevilacqua, A. J. Durkin, and B. J. Tromberg, "Modulated imaging: quantitative analysis and tomography of turbid media in the spatial-frequency domain," Opt. Lett. **30**(11), 1354–1356 (2005).
22. S. D. Konecky, A. Mazhar, D. Cuccia, A. J. Durkin, J. C. Schotland, and B. J. Tromberg, "Quantitative optical tomography of sub-surface heterogeneities using spatially modulated structured light," Opt. Express **17**(17), 14780–14790 (2009).
23. A. Mazhar, D. J. Cuccia, S. Gioux, A. J. Durkin, J. V. Frangioni, and B. J. Tromberg, "Structured illumination enhances resolution and contrast in thick tissue fluorescence imaging," J. Biomed. Opt. **15**(1), 010506 (2010).
24. J. R. Weber, D. J. Cuccia, A. J. Durkin, and B. J. Tromberg, "Noncontact imaging of absorption and scattering in layered tissue using spatially modulated structured light," J. Appl. Phys. **105**(10), 102028 (2009).
25. J. R. Weber, D. J. Cuccia, W. R. Johnson, G. H. Bearman, A. J. Durkin, M. Hsu, A. Lin, D. K. Binder, D. Wilson, and B. J. Tromberg, "Multispectral imaging of tissue absorption and scattering using spatial frequency domain imaging and a computed-tomography imaging spectrometer," J. Biomed. Opt. **16**(1), 011015–011017 (2011).
26. S. D. Konecky, T. Rice, A. J. Durkin, and B. J. Tromberg, "Imaging scattering orientation with spatial frequency domain imaging," J. Biomed. Opt. **16**(12), 126001 (2011).
27. S. D. Konecky, C. M. Owen, T. Rice, P. A. Valdés, K. Kolste, B. C. Wilson, F. Leblond, D. W. Roberts, K. D. Paulsen, and B. J. Tromberg, "Spatial frequency domain tomography of protoporphyrin IX fluorescence in preclinical glioma models," J. Biomed. Opt. **17**(5), 056008 (2012).
28. T. B. Rice, S. D. Konecky, A. Mazhar, D. J. Cuccia, A. J. Durkin, B. Choi, and B. J. Tromberg, "Quantitative determination of dynamical properties using coherent spatial frequency domain imaging," J. Opt. Soc. Am. A **28**(10), 2108–2114 (2011).
29. A. Mazhar, D. J. Cuccia, T. B. Rice, S. A. Carp, A. J. Durkin, D. A. Boas, B. Choi, and B. J. Tromberg, "Laser speckle imaging in the spatial frequency domain," Biomed. Opt. Express **2**(6), 1553–1563 (2011).
30. P. Zakharov, A. Völker, A. Buck, B. Weber, and F. Scheffold, "Quantitative modeling of laser speckle imaging," Opt. Lett. **31**(23), 3465–3467 (2006).
31. P. Zakharov, A. C. Völker, M. T. Wyss, F. Haiss, N. Calcinaghi, C. Zunzunegui, A. Buck, F. Scheffold, and B. Weber, "Dynamic laser speckle imaging of cerebral blood flow," Opt. Express **17**(16), 13904–13917 (2009).
32. A. B. Parthasarathy, W. J. Tom, A. Gopal, X. Zhang, and A. K. Dunn, "Robust flow measurement with multi-exposure speckle imaging," Opt. Express **16**(3), 1975–1989 (2008).
33. J. W. Goodman, *Speckle phenomena in optics: theory and applications* (Roberts & Co., Englewood, Colo., 2007), pp. xvi, 387 p.
34. P. A. Lemieux and D. J. Durian, "Investigating non-Gaussian scattering processes by using nth-order intensity correlation functions," J. Opt. Soc. Am. A **16**(7), 1651–1664 (1999).
35. S. J. Kirkpatrick, D. D. Duncan, and E. M. Wells-Gray, "Detrimental effects of speckle-pixel size matching in laser speckle contrast imaging," Opt. Lett. **33**(24), 2886–2888 (2008).
36. A. A. Middleton and D. S. Fisher, "Discrete scatterers and autocorrelations of multiply scattered light," Phys. Rev. B Condens. Matter **43**(7), 5934–5938 (1991).

37. G. Maret and P. E. Wolf, "Multiple light scattering from disordered media. The effect of brownian motion of scatterers," Z. Phys. B Condens. Matter **65**(4), 409–413 (1987).
38. L. Wang, S. L. Jacques, and L. Zheng, "MCML–Monte Carlo modeling of light transport in multi-layered tissues," Comput. Meth. Prog. Bio. **47**(2), 131–146 (1995).
39. D. D. Duncan, S. J. Kirkpatrick, and R. K. Wang, "Statistics of local speckle contrast," J. Opt. Soc. Am. A **25**(1), 9–15 (2008).
40. J. C. Hebden, B. D. Price, A. P. Gibson, and G. Royle, "A soft deformable tissue-equivalent phantom for diffuse optical tomography," Phys. Med. Biol. **51**(21), 5581–5590 (2006).
41. B. W. Pogue and M. S. Patterson, "Review of tissue simulating phantoms for optical spectroscopy, imaging and dosimetry," J. Biomed. Opt. **11**(4), 041102–041116 (2006).
42. F. Ayers, A. Grant, D. Kuo, D. J. Cuccia, and A. J. Durkin, "Fabrication and characterization of silicone-based tissue phantoms with tunable optical properties in the visible and near infrared domain," Proc. SPIE 687007 (2008).

1. Introduction

Dynamic Light Scattering (DLS) techniques are widely used to characterize particle motion and flow [1–3]. In general, the method relates the decay of the autocorrelation function of coherent light to the speed of rough surfaces or scattering particles. Several DLS methods are employed in biomedical research, including: Laser Doppler flowmetry [4–6], Diffusing Wave Spectroscopy (DWS) [7–10], and Laser Speckle Imaging (LSI) [11–16]. These techniques have historically been limited to qualitative, relative flow metrics due to reliance on approximations, such as single photon scattering, to determine the autocorrelation function.

An important modeling advancement for DLS in turbid media is the idea that the electric-field temporal autocorrelation function $G_1(\tau) = <E(0)E*(\tau)>$ obeys a transport equation [17]. Thus, the autocorrelation function can be found as a function of source-detector separation, for example, using familiar transport solver techniques such as diffusion or Monte Carlo [10]. Making use of the Siegert relation, the field autocorrelation function can be related to the experimental realizable intensity autocorrelation in order to determine the dynamics of light scattering structures [12]. Measurement of the intensity autocorrelation is relatively straightforward for fiber based techniques such as DWS, where the temporal resolution is fine and the distance between the source and detector is clearly defined. In contrast, image based measurements such as LSI generally require longer exposure times and ill defined source-detector elements. However, by performing radial Hankel Transforms on results from transport models, one can instead find autocorrelation as a function of *spatial frequency* [18]. The planar nature of Fourier basis functions are naturally well suited for two-dimensional imaging.

Structured light concepts have been applied to the transport of light intensity as the foundation for a reflectance imaging technique called Spatial Frequency Domain Imaging (SFDI). SFDI has been well established to determine the absorption, scattering, and fluorescent properties in turbid media [19–26]. Using structured light also allows for a tomographic reconstruction of layered, heterogeneous optical properties [22, 27], because the depth penetration of the light depends on the spatial frequency of projection.

In a previous manuscript, we applied experimental methods and modeling precedent from SFDI to the transport of *correlation* by projecting structured *coherent* light on dynamic scattering objects, and measuring the speckle contrast as a function of spatial frequency [28]. We showed that the speckle contrast follows expected behavior as a function of spatial frequency [29], and that correctly modeling the effect using correlation transport allows one to fit quantitatively for the flow properties of light scattering particles in a homogenous medium [28].

In a biological setting, samples are often layered and heterogeneous. Thus, planar speckle images are formed from photons that may interact with scatterers of different flow dynamics. This issue has been recognized and addressed for samples composed of a static scattering layer above a dynamic layer [30]. Here, the presence of a static top layer introduces non-ergodic speckle fluctuations, which affect fitted flow values. To rectify non-ergodic data, the

field autocorrelation was re-derived assuming a superposition of fields from photons scattered by static and dynamic particles [15, 30]. At least one additional image exposure must be taken to separate the dynamic field component. This method has been used successfully in phantoms and in-vivo [31, 32], but the method falls short in some aspects: it does not account for photons that scatter partially in both static and dynamic regions, and it cannot determine the presence of static scatterering layers *beneath* the sample surface nor situations where both layers are dynamic, but with different flow rates or types (e.g. a large vessel buried beneath a capillary network). Our manuscript demonstrates a method that overcomes these limitations by incorporating multiple exposures and spatial frequencies into the speckle contrast measurement. With this method, we are able to determine quantitative flow properties in multi-layered media.

2. Theory

LSI measures speckle contrast, which is defined as:

$$K = \frac{\sigma}{<I>}, \tag{1}$$

where K is the speckle contrast, σ is the intensity standard deviation, and $<I>$ is the mean intensity. This calculation is generally performed using a sliding window filter across the raw speckle image, which then generates a speckle contrast image. For a speckle pattern with some finite integration time T, K is related to the electric field autocorrelation function $G_1(\tau)$ through the expression [14, 33]

$$K^2 = \frac{2\beta^2}{T} \int_0^T (1 - \frac{\tau}{T}) \left| \frac{G_1(\tau)}{G_1(0)} \right|^2 d\tau. \tag{2}$$

Here β represents a multiplicative reduction in contrast not associated with the dynamics of the scatterers, such as depolarization, coherence length, or mismatch between the image pixel and speckle size [34, 35]. For turbid media, a correlation diffusion equation can be used to find G_1 analytically as a function of optical properties and the mean square displacement $<\Delta r^2(\tau)>$ [10]. However, we and others have shown that when imaging speckle over a wide field, the diffusion approximation breaks down more readily because of shorter average photon path lengths and relatively long camera exposure times [28, 30]. Therefore, we utilize Monte Carlo (MC) simulation techniques to determine the autocorrelation function. As proposed in [9, 10, 36], the autocorrelation can be found as a function of separation from a point light source, ρ, by tracking the momentum transfer distribution at discrete ρ bins and numerically integrating over the single scattering decorrelation exponential [37]. The minimum bin resolution determines the maximum spatial frequency able to be modeled without aliasing. In our case we use $\Delta\rho = 0.1$ mm, which according to Nyquist yields $f_{max} = 1/2\Delta\rho = 5$ mm^{-1}, easily sampling our intended maximum spatial frequency of 0.25 mm^{-1}:

$$G_1(\tau, \rho_i) = \int_0^\infty P(Y, \rho_i) \exp\left[\frac{-k_0^2 Y \langle \Delta r^2(\tau) \rangle}{3} \right] dY. \tag{3}$$

Here $P(Y)$ is the distribution of dimensionless momentum transfer, $Y = 1-cos(\theta)$, k_0 is the wave number inside the medium, and $<\Delta r^2(\tau)>$ is the mean-squared displacement. Because MESI affords us the opportunity to fit for the *type* of motion (diffusive or directed flow), we choose to write the displacement in terms of its flow coefficient and temporal power: $<\Delta r^2(\tau)> \equiv Vt^n$. Here n can take integer values of one or two. A value of $n = 1$ indicates diffusive flow where V would represent six times the Brownian Diffusion Coefficient D_b. A

value of $n = 2$ represents directional flow where V would represent the square of the particle velocity.

Handling multiple layers adds extra difficulty because the decorrelation exponential is a nonlinear function of both the total momentum transfer Y and also the *fractional momentum transfer distribution in each layer for that Y*. The autocorrelation becomes a multi-integral, which for a two layer (or three layer with identical 1st and 3rd layer) system can be written using conditional probabilities:

$$G_1(\tau, d, \rho_i) = \int_0^\infty P(Y, d, \rho_i) \int_0^1 P(y \mid d, \rho_i) \exp\left\{ \frac{-k_0^2 Y \left[V_1 t^{n_1}(y) + V_2 t^{n_2}(1-y) \right]}{3} \right\} dy \, dY. \quad (4)$$

Here y is the fraction of Y originating from the first layer, d is the first layer depth, and V_1, V_2 are the flow coefficients of the first (or first and third) and second layer, respectively. Note that the conditional probability distribution $P(y|\rho)$ must be generated for each value of the source-detector separation ρ_i (or momentum transfer). We choose a two-layer system as the simplest case, but the method can be extended for arbitrary numbers of layers. However, each additional layer increases the number of conditional probability distributions required by another power.

It is important to realize that the approximation for speckle contrast in the presence of static scatterers, as presented in [10, 30, 32, 34], can be re-derived using our formalism by assuming that the conditional probability is separable and equivalent to $P(y|\rho) = w\delta(0) + (1-w)\delta(1)$, where the weighting factor w is the usual ratio of dynamic to static intensity $\langle I_f \rangle / (\langle I_f \rangle + \langle I_s \rangle)$. This is equivalent to assuming that the speckle contrast arises from photons that scatter *only* in static *or* dynamic layers, but not both. Clearly, numerous photons scatter multiply through both layers, hence we feel the full distribution must be calculated and integrated to increase accuracy of the model.

To find the autocorrelation as a function of *spatial frequency,* one can apply a numerical Hankel Transform to G_1 [28]

$$G_1(\tau, d, f) = 2\pi \int_0^\infty G_1(\tau, d, \rho) J_0(2\pi f \rho) \rho \, d\rho. \quad (5)$$

Finally, the speckle contrast modulation transfer function $K(f)$, can be found by inserting G_1 into Eq. (2). $K(f)$ is the expected speckle contrast for each spatial frequency when the coherent source has *spatial structure*. Note the order of Eq. (4)-(5) is arbitrary, as the Hankel Transform can be applied to $P(Y,\rho)$, then integrated. Note also the derivation here is done in terms of continuous variables and integrals, but were performed numerically using results provided by Monte Carlo methods.

Potential parameters that can be found when fitting to combined multi-exposure and multi-frequency data include: V_1, V_2, d, n_1, n_2.

3. Methods

A multi-layer C# based Monte Carlo application was downloaded from the Virtual Photonics Technology Initiative (http://www.virtualphotonics.org/). This application tracks photon weight and momentum transfer as a function of layer and optical properties using standardized Monte Carlo RTE solver methodology [38]. Histograms were generated using one million photons, at appropriate optical properties, for the total and fractional momentum transfer, $P(Y,\rho)$ and $P(y|\rho)$, respectively. These results were Hankel Transformed and numerically integrated using Matlab (Mathworks, Inc) software to give predicted $K(f)$.

Validation experiments were performed using a structured light imaging system shown in Fig. 1. A stabilized 45 mW 687nm diode laser (Ondax, Inc), with coherence length exceeding 1 m, was passed through a sinusoidal film slide (0.2 mm^{-1}, Applied Image Inc.), and projected

through a series of focusing optics onto the sample surface. The optics kept the field of projection constant, and the frequency was changed by translating the stage along the divergent source axis. Images were captured with a Retiga EXI cooled 12-bit CCD camera (Qimaging, Inc), equipped with a 200 mm focal length lens set at F16, giving a field of view approximately 8 mm by 6 mm. The optical imaging axis was angled slightly (~10 degrees) to avoid specular reflection. A cross polarizer was also placed in the camera lens to help further reject specular light and increase speckle contrast.

To determine speckle contrast as a function of spatial frequency we take advantage of the demodulation scheme described in [20]. This technique allows one to isolate the intensity *I* (or standard deviation) amplitude of a single frequency component by combining images at three equally separated phases $\varphi_{1,2,3} = (0, 2\pi/3, 4\pi/3)$ such that:

$$I_i = I_{DC} + I_{AC} \cos\left(2\pi f x + \varphi_i\right) =>$$

$$I_{AC} = \frac{\sqrt{2}}{3}\left[\left(I_1 - I_2\right)^2 + \left(I_2 - I_3\right)^2 + \left(I_1 - I_3\right)^2\right]^{1/2} \tag{11}$$

The amplitude of the standard deviation maps can be calculated in the same manner as it scales linearly with intensity. The contrast is then simply $K_{AC} = \sigma_{AC}/I_{AC}$. Standard deviation and mean maps were calculated using a small sliding window filter of 7x7 pixels. Border areas within 7 pixels of the edge were discarded. A window size of 7x7 is typical in the literature, and chosen as a reasonable compromise between spatial resolution and increased sampling statistics [39]. All measurements were carefully designed to meet or exceed Nyquist criteria and minimize sampling errors [35]. The value of β was found empirically using a static diffusive target and calculated to be $\beta = 0.81$.

A variety of static and dynamic phantoms were created to validate our models. Static phantoms were created at varying thicknesses using silicone PDMS. Titanium dioxide was used as a scattering agent, and India ink provided absorption. Phantom thickness was set by shallow molds and verified using calipers. The optical coefficients for static phantoms at 685 nm light were set at approximately $\mu_s' = 1.2\ mm^{-1}$, $\mu_a = 0.005\ mm^{-1}$, based on known values for these substances [40–42]. Dynamic liquid phantoms were created using polystyrene microspheres of diameter 800 nm (Spherotech, Inc.) as a scattering agent, and India ink. Using the Stokes-Einstein equation for diffusion of spheres in liquid, the diffusion coefficient was calculated to be $D_b = 6.1x10^{-7}\ mm^2/s$. The scattering coefficient for liquid phantoms at 685 nm was set at $\mu_s' = 0.6\ mm^{-1}$, using an appropriate concentration of microbeads. This concentration was determined by theoretical Mie scattering calculations, conveniently provided by the Oregon Medical Laser Center (http://omlc.ogi.edu/calc/mie_calc.html). Absorption was set at $\mu_a = 0.005\ mm^{-1}$.

Phantom experiments were conducted in three separate test configurations shown in Fig. 1.
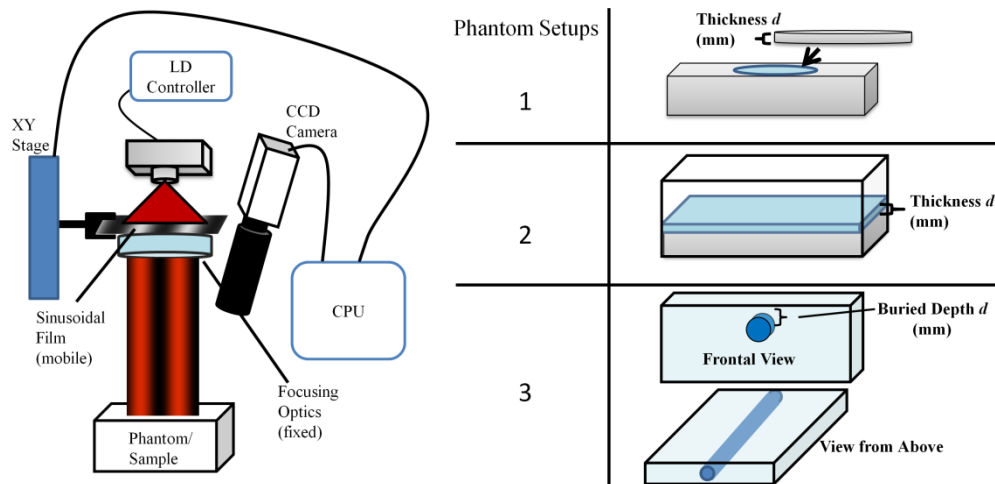
Fig. 1. (Left) Experimental setup for laser speckle imaging with structured light. Spatial frequencies are set by the (vertical) distance between the sinusoidal film and divergent laser diode. The film is moved horizontally to change the phase. (Right) Three phantom validation setups to test our models: (1) static layer above dynamic layer, (2) dynamic layer above static layer, and (3) diffusing dynamic layer above flowing dynamic layer.

First, thin static phantoms were placed over a semi-infinite well of dynamic phantom. The layer thickness was varied from 0.4 to 4 mm. This setup was designed to be comparable with previous experiments using MESI to account for static speckle layers [30].

Second, a thin liquid phantom was poured into a container *above* a semi-infinite layer of *static* phantom. The layer thickness was varied from 0.75 mm-3.75 mm. For thin liquid layers under 1 mm, a small amount of dish soap (~1 drop) was added to reduce surface tension and decrease beading. The soap was found to have insignificant impact on solution viscosity and optical coefficients. This particular setup was designed to illustrate where the MESI method falls short due to its reliance on static speckles in each image remaining constant with exposure time. For a dynamic top layer, nearly all photons interact with dynamic scatterers but are still significantly influenced by static sections below.

Third, a dynamic scattering liquid was confined in a clear polyurethane tube of radius 2 mm, pumped at a known flow rate, and submerged in a container full of an identical scattering liquid (at rest). The flow rate was controlled with a syringe pump (New Era Pump Systems Inc.) and varied from 0.375 mm/s-1.88 mm/s. The depth of the submerged tube was fixed at 1.25mm. MESI methods designed to account for static speckle contrast would also fail in this situation since both layers are dynamic. The (relatively) slow Brownian diffusion of the top layer dilutes the overall speckle contrast considerably when compared to the fast, directional flow in the tube.

Experimental data for all configurations were collected at 10 exposure times evenly spaced between 0.5 and 14 ms. These values were chosen to maximize the "S" sensitivity curve of speckle contrast to exposure time at our dynamics of interest (i.e. Brownian Motion and Flow < 2 mm/s), as predicted by literature values and forward simulation [30, 32]. For configuration one, six spatial frequencies were imaged between 0 and 0.25 mm^{-1}. For configuration two and three, five spatial frequencies were recorded between 0 and 0.12 mm^{-1}. In each case these frequency bounds were chosen to maximize sensitivity of the speckle contrast measurement, with higher frequencies eliminated as they approach an asymptote in the momentum transfer distribution. The number of frequencies and exposures was chosen as a compromise between time of measurement and accuracy. Note the minimum number must exceed the number of unknowns, while the optimal number is still unknown and requires further study.

After images were recorded, speckle contrast data was averaged across the image at all frequencies for phantom configurations one and two, and then fit as a single data point. Fits were performed using a non-linear least squares solver for *combined* multi-exposure and spatial frequency data. Four parameters were fit: velocity coefficients V_1, V_2, the temporal displacement powers n_1, n_2, and the top layer thickness d. For configuration 3, speckle contrast data was binned to a size of 39 by 29 pixels and fits performed for each individual pixel. Sub-regions of interest were then chosen and the fits averaged. Fits were performed in two steps: first, multi-exposure high spatial frequency content (>0.1 mm^{-1}) was used to find V_1 and n_1 outside the tube region, where homogeneity can be assumed. Here the shorter mean path lengths of high frequency content served to reduce partial volume effects caused by the tube. Once V_1 was fit, this variable was fixed in the least squares solver and planar multi-exposure content (0 mm^{-1}) was used to fit for V_2, n_2, and d.

4. Results

Momentum transfer probability distributions as a function of spatial frequency, generated by our Monte Carlo model for $\mu_s' = 0.6$ mm^{-1}, $\mu_a = 0.005$ mm^{-1}, are shown in Fig. 2.
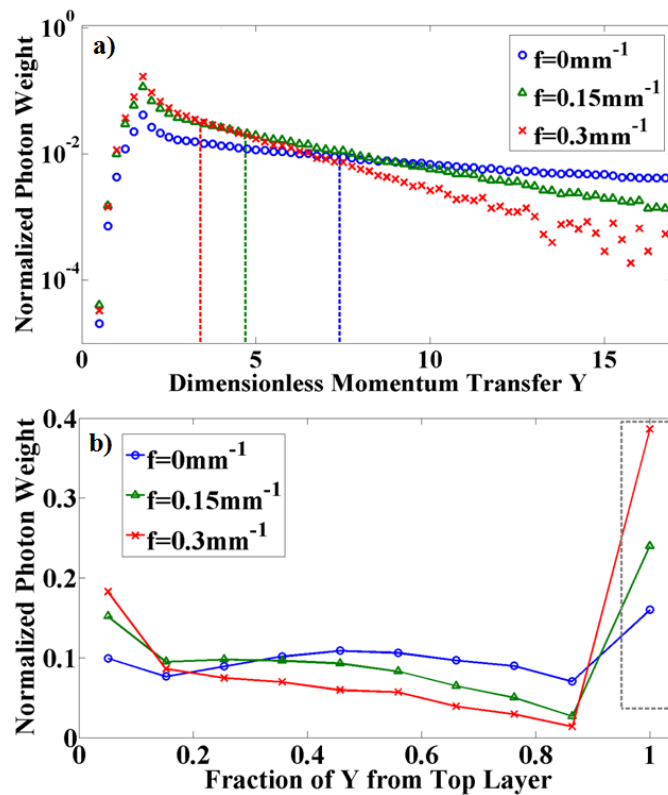

Fig. 2. (a) Photon weight probability distribution for total momentum transfer $P(Y,f)$. Dotted lines represent the mean momentum transfer for each spatial frequency. Note the increase in mean momentum transfer with low spatial frequency. Some noise is visible at high spatial frequencies and momentum transfers due to insufficient Monte Carlo sampling, but due to small weights here was found to have insignificant effect on calculated speckle contrast values. (b) Layer-specific fractional momentum transfer $P(y|f)$. Here we see a relatively constant probability among all fractions, up to the abrupt discontinuity highlighted by the dotted rectangle, which represents photons that *do not reach the bottom layer*. These photons create large non-ergodic effects, which are naturally accounted for using the Monte Carlo method.

The probability distributions illustrate significant change in momentum transfer and depth penetration with spatial frequency, which is the driving force behind our technique. This dependence is used to fit speckle contrast at multiple exposures and spatial frequencies to quantitative, layered flow values.

Figure 3 shows experimental speckle contrast with corresponding fits for phantom configurations one and two.
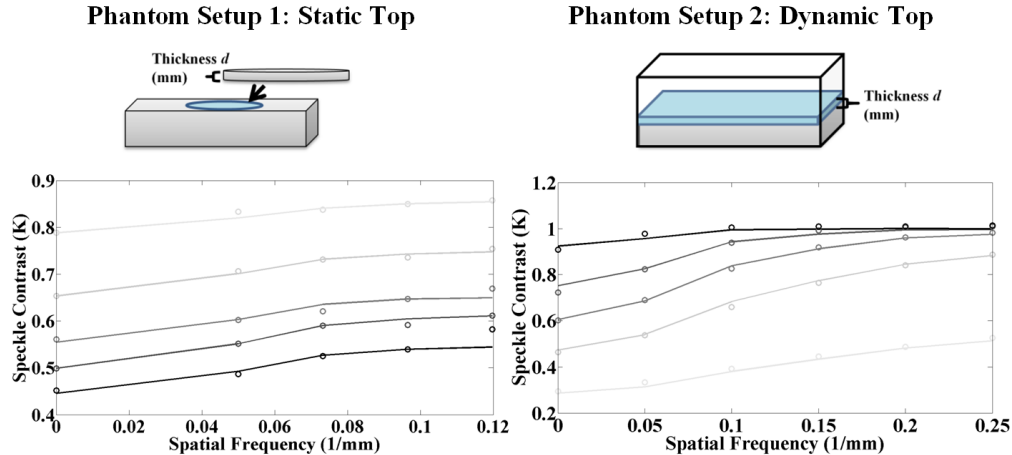

Fig. 3. Validation phantom speckle contrast fits for configurations 1 and 2. Experimental speckle contrast measurements (circles) and subsequent fits (solid line) for five values of thickness d, linearly spaced between 0.7mm (lightest) and 3.0mm (darkest). Notice the drastic difference between the shape of the speckle contrast curve, as low frequencies tend to average both layers, and high frequencies tend toward the dynamics of the top layer.

Figure 4 shows fit values corresponding to phantom setups one and two. Note that temporal displacement power n was fit as $n = 1$ for both cases. Thus, the flow coefficient here is equivalent to six times the Brownian Diffusion Coefficient D_b. While the static layer diffusion coefficient is expected to be zero, this value cannot be reached by the fitting algorithm once it becomes arbitrarily small and ceases to affect the contrast. We define this "effective zero" as the point when there is < 3% difference between the effective and actual zero speckle contrast. The effective zero depends on layer thickness.

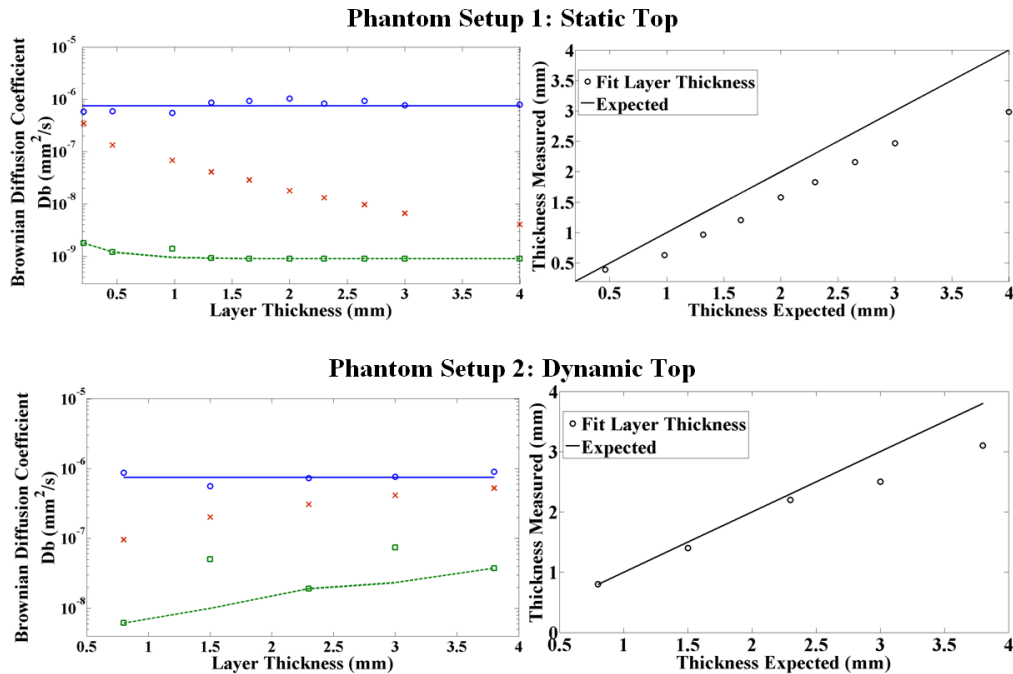**Phantom Setup 1: Static Top**

Phantom Setup 2: Dynamic Top

Fig. 4. Fitted values V_1, V_2, d for phantom configurations one (top) and two (bottom). Recovered n values were found to be one in both cases, and thus we define the flow coefficient as six times the Brownian Diffusion Coefficient D_b. Multi-layer fits for dynamic phantom D_b (circles) and static phantom (squares) are shown alongside blind single layer fits (x's) and expected values (solid and dashed lines). Blind fits can be seen to vary significantly, over two orders of magnitude in some cases, from expected values. Notice the effective zero line (dashed) depends on layer thickness and depends heavily on the phantom geometry. Depth fits generally underestimate true values by a small margin.

An exploration into partial volume effects, and subsequent reasoning behind the two-step fitting process for phantom configuration three is shown in Fig. 5. Here the speckle contrast image at $f = 0\ mm^{-1}$ is shown, and Region of Interest (ROI) highlighted in a portion of the image expected to be homogenous. Mean speckle contrast in this ROI is calculated for $f = 0\ mm^{-1}$ and $f = 0.12\ mm^{-1}$, and compared with measurements made on a truly homogenous sample with no tube present. As can be seen from Fig. 5, at $f = 0\ mm^{-1}$ speckle contrast differs substantially from a true homogenous sample, and that difference increases with tube velocity. This is due to the fact that at low projection frequencies, the relatively long average optical path lengths allow a significant fraction of the detected light to interact with the tube [20]. In contrast, high projection frequencies reduce the mean optical path length, and there is essentially no detectable contribution from the deeper dynamic structure. Thus, to increase accuracy and effective resolution, flow coefficients and flow types for the surrounding medium, V_1 and n_1, are fit using exclusively high frequency data.

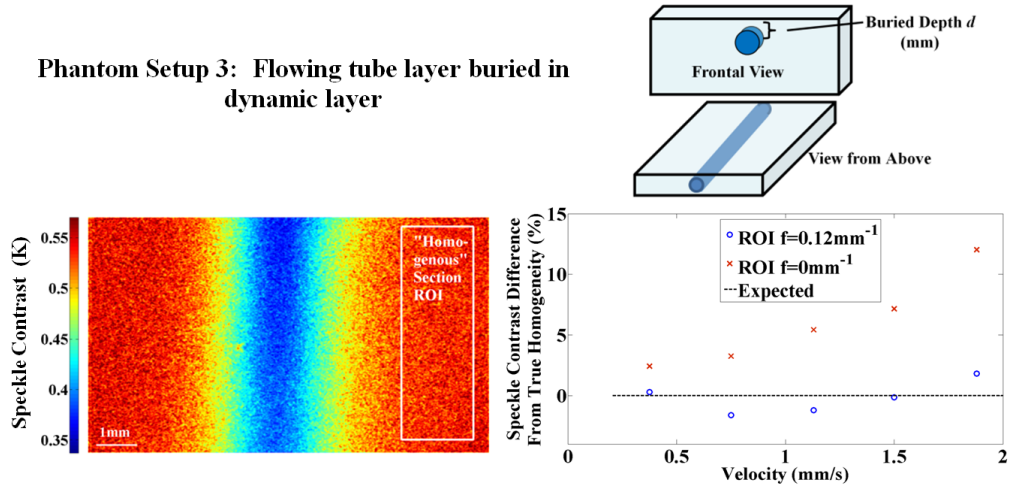**Phantom Setup 3: Flowing tube layer buried in dynamic layer**

Fig. 5. Experimental speckle contrast image for DC spatial frequency (*0 mm^{-1}*), and representative ROI for "homogenous" regions (left). The region appears uniform but is actually highly dependent on tube velocity for low spatial frequencies, as shown in the plot (right). Here, the DC frequency (x's) varies by as much as 13% from a truly homogenous sample. The AC (circles) spatial frequency (*0.12 mm^{-1}*), in contrast, is not heavily influenced by tube velocity due to lower average path lengths.

Figure 6 shows multi-exposure fitting results at a range of tube velocity values. Fitted speckle contrast for both "homogenous" sections and high flow "tube" sections of each image are shown in Fig. 6(b). Fit variables V_2, n_2, and d, are shown in Fig. 6(c), 6(d), and 6(e), and performed using multi-exposure data at $f = 0$ mm^{-1} and previous high frequency fits for V_1 and n_1, described above. The fits are averaged for the two given ROI's.
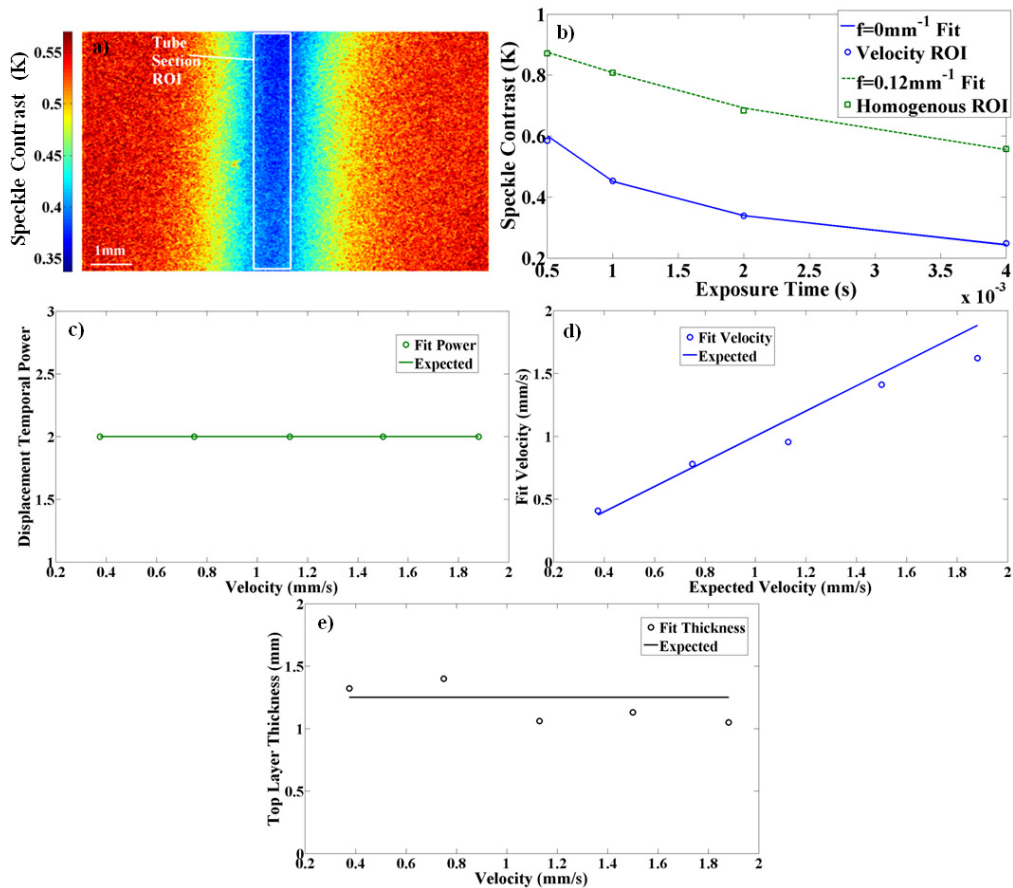
Fig. 6. Validation phantom results for configuration 3. Raw speckle contrast is shown in (a), with an ROI chosen to highlight the high flowing tube region. Fitted contrast values for both ROI's are shown at one exposure (0.5 ms) in (b). Averaged fits for n_2 (c), V_2 (d), and d (e), show good agreement with expected values based on syringe pump settings and caliper measurements of flow and thickness. Because n_2 is restricted to integer values, the fit shows perfect agreement with the expected power of two for directional flow. Therefore, V_2 is defined as the flow *velocity*.

Note that in more complicated samples, there may not be a clearly identifiable "homogenous" region, but the operating principle is still exceedingly useful. Essentially, high spatial frequencies gate diffuse photon components from the measurement, and allow for the isolation of surface flow. We believe this information to be valuable in any speckle image fitting process.

5. Discussion and conclusion

A method for fitting speckle contrast to quantitative flow in layered geometries was shown, which combined features of Monte Carlo modeling, multi-exposure speckle imaging, and spatial frequency domain analysis. To model this process correctly, a key data feature must be tracked in our Monte Carlo algorithm: layer-specific fractional momentum transfer distribution. This distribution shows a dependence of "momentum transfer penetration depth" on spatial frequency, where higher spatial frequencies penetrate less into a scattering medium. Useful parameters such as flow coefficients and temporal displacement power also depend strongly on exposure time. Thus, we structured coherent light and measured contrast at several exposures to take advantage of these complementary effects. Using controlled

phantom experiments with known flow values in three different geometries, we showed that all parameters of interest could be fit accurately to speckle contrast maps.

Translating this method to biological samples will admittedly present extra complications, as these are typically composed of multiple intersecting layers with highly variable flow speeds. However, incorporating multiple spatial frequencies and exposure times into speckle imaging provides researchers necessary additional elements of control in the sampled photon path length and sensitivity to flow speeds present in a sample volume. By investigating the potential fitting power behind this additional information content, our manuscript represents a building block towards biological applicability. We believe that with the advent of more advanced imaging sensors, lasers, and Monte Carlo solvers, researchers will be able to quantitatively image flow in a substantially broader range of conditions.

In ongoing research, we plan to expand our technique to in-vivo tissue studies. Important applications include measuring blood flow and metabolism in pre-clinical rodent brain models, retina, and skin. In each of these cases the presence of layered structures with varying optical properties can have a sizeable impact on the measured speckle contrast. We hope to combine optical absorption tomography and layered speckle measurements for a more accurate rendering of metabolic tissue function.

Acknowledgments